

# Decentralized control of islanding/grid-connected hybrid DC/AC microgrid using interlinking converters

Diress Tilahun Antalem\* , Muneer V , and Avik Bhattacharya

Indian Institute of Technology Roorkee, Haridwar 247667, India

Received: 1 April 2022 / Accepted: 7 October 2022

**Abstract.** This paper presents decentralized control of an islanding/grid-connected DC/AC hybrid microgrid ( $\mu$ G) using battery energy storage system (BESS) and distributed energy resource (DER). In DC/AC  $\mu$ G unified with different DERs and BESS, the intermittent output nature of DERs due to fluctuating input characteristics and strong interaction of sources, loads, and primary grid, causes variations in frequency and bus voltage. To solve these issues, the paper proposes a decentralized control method which incorporates active/reactive power ( $P/Q$ ) control, DC virtual droop control, voltage control, frequency droop control, current control, maximum power point tracking, and a phase-locked loop (PLL). The coordination and integration of various control parameters will ensure a smooth transition as well as the overall stability of the system. The BESS and DER's interfacing converters are autonomously controlled in this control scheme without communication using the frequency droop and bus voltage control. Correspondingly, the control techniques comprehend different operating modes depending on the state of charge of BESS, distributed generation, and grid. During switching the two interlinking converters (IC), high-frequency harmonics are created, which are eventually mitigated by the inductor-capacitor-inductor (LCL) filters employed in the AC bus. Virtual droop control will ensure active damping of the harmonics in the LCL network. The maximum power transfer in interlinking converters (ICs) is improved using the proposed approach for input-source variations. Simulations were performed using MATLAB/Simulink and verified using the hardware in the loop (HIL) to prove the effectiveness of the control scheme proposed.

**Keywords:** DC/AC microgrid, Decentralized control, Distributed energy resource, Frequency droop control, MPPT,  $P/Q$  control.

## Nomenclature

DER	Distributed Energy Resource	$T_m$	Turbine torque
$\mu$ G	Microgrid	$V_{\text{wind}}$	Wind speed
BESS	Battery Energy Storage System	$A$	Turbine area
MPPT	Maximum Power Point Tracking	$\omega$	Turbine rotational angular frequency
PLL	Phase-locked Loop	$C_p$	Power coefficient
IC	Interlinking Converter	LPF	Low Pass Filter
DC	Direct Current	$F$	Feedforward
AC	Alternating Current	$i_{\text{Ld ref}}$	Reference current of the direct axis
DG	Distributed Generation	$i_{\text{Lq ref}}$	Reference current of the quadrature axis
MPPV	Maximum Power Point Voltage	$L_f$	Filter inductor on the inverter side
$P_{\text{batt}}$	Battery power	$C_f$	Filter capacitor
$P_m$	Mechanical power generated by wind	$L_c$	Filter inductor on the grid side
$C_q$	Torque coefficient	$\omega_{\text{res}}$	Resonant frequency
$\lambda$	Tip speed	$R_d$	Passive damping
		SRF	Synchronous Reference Frame
		$\delta$	Duty cycle
		HIL	Hardware in the loop
		$V_{cf}$	Filter capacitor voltage

\* Corresponding author: [t.diress@yahoo.com](mailto:t.diress@yahoo.com)

SOC	State Of Charge
PCC	Point of Common Coupling

## 1 Introduction

The antithetical relationship between continuously increasing demand for energy and consequent degradation of the environment has triggered electric power experts to search for a feasible asset to mitigate the issues in power generation. Distributed energy resources, like wind and solar power with advanced power electronics technologies and control techniques, are believed to bring out a practical solution to scale down dependence on the conventional electric power procreation and increase the reliability feature of a power system [1, 2]. Emerging solar photovoltaic technology, wind technology growth, and declining tariff also motivate rapid solar photovoltaic (PV) and wind deployment in a power system. Nevertheless, considering the character of wind energy and solar energy, the momentary output power of wind and solar systems highly depends on the operating atmospheric elements, such as wind speed, the surrounding temperature, and solar irradiance resulting in variable output power [3]. Therefore, the BESS incorporated in the proposed DC/AC microgrid addresses the issue of irregularity and increases the microgrid stability, power quality, and reliability [4, 5]. When distributed energy resources operate autonomously with the central ac grid, they may cause voltage and frequency variation [6]. To overcome these variations in the autonomous or grid-connected mode, an efficient voltage controller, a power controller, a frequency droop controller, a current controller, and a  $P/Q$  controller design were proposed to ensure the microgrid's satisfactory operation. Interlinking converters are used for renewable energy source changeover from DC to AC output, either connected in utility grid or autonomous modes [7]. The optimally designed inductor–capacitor–inductor (LCL) filter is deployed to reduce the harmonic output current between interlinking converters and the utility, and it also imposes a performance current for feedback control [8]. This filter allows using a lower switching frequency to accommodate harmonic restraint mentioned in IEEE-1547 and IEEE-519 standards [9].

A hybrid DC/AC microgrid ( $\mu$ G) is a vital technology for the assimilation of DERs, and energy storage (BESS) to provide reliable power to a bundle of local loads correlated to pure DC or AC microgrids [10]. A hybrid DC/AC  $\mu$ G can serve either in an islanding or a grid-interactive mode [11]. In grid interactive applications, the  $\mu$ G actively controls reactive power with voltage regulation, power quality improvement, and active power dispatch to improve further efficient utilization of BESSs and DERs [12].

In the grid-connected operation, parallel ICs are used for DC voltage control; the DERs output can decide the interlinking converter power, discharge/charging power of BESSs, and manage the demand in the DC  $\mu$ G. In the autonomous mode, frequency, voltage at the DC-bus, and three-phase AC voltage can be controlled through synchronous control of the BESSs, ICs, and DERs in the hybrid DC/AC microgrid [11, 13].

In [14], to coordinate parallel ICs operation, centralized control is implemented in a DC  $\mu$ G. The control scheme, a predictive-model strategy, is used for load allocation and voltage control. The prevailing lack of the centralized method is the scarcity of reliability, vulnerability to a single point breakdown, and flexibility. In [15] proposed, a master slave-based load sharing control with wireless analog communication. It has an identical drawback to a central method in the fact that master-slave failure results in a deficit of voltage regulation. In the hybrid, DC/AC microgrid, different power electronic converters interface DERs and regulate the electrical parameters among sources and loads [16]. Communication-based coordination control and supervisory control are studied in a networked hybrid microgrid in [17–19]. However, costly communication lines among modules reduce microgrid reliability limits and DER's flexibility and expansion. In [20], an autonomous hybrid microgrid with coordination control operations were studied. However, there is a crucial challenge in administering the power flow between all distributed sources. Nowadays, well-established droop control, including different alternatives suggested in the literature, is primarily for ac microgrids [21, 22]. The droop method expansion to hybrid DC/AC  $\mu$ G has not been widely explored. It could be roughly complex since it extends across at least two subgrids having DC and AC forms. In [23], low switching frequency harmonic current rejection in DC/AC microgrid topology was studied in islanding and grid-connected mode. However, the power quality and correct power-sharing approaches between DERs need more improvements. In [24], adaptive power-sharing and sliding mode control are used. However, the microgrid DC-link voltage stability is not addressed. Amirkhan et al. [25] proposed a sliding mode surface control and two-dimensional impedance shaping technique. These control techniques work with nonlinear systems. But, there is an uncertainty effect due to parameter variations and chattering problems.

The proposed microgrid architecture consists of both DC subgrid and AC grid, avoiding communication lines, accurate power-sharing, and significant improvement of the power quality is achieved.

An essential DC/AC hybrid  $\mu$ G architecture is demonstrated in Figure 1. The renewable sources are interconnected with permanent magnet synchronous generator (PMSG) wind turbines and PV arrays with a series-parallel combination of solar panels. The hybrid microgrid topology also comprises of solar DC–DC unidirectional converter, LCL filter, energy storage battery bank, interlinking converter, DC–DC bi-directional converter, uncontrolled rectifier, wind DC–DC converter, AC primary grid, controller, DC load, and constant power loads. A DC to DC unidirectional converter controls the power generated from wind and solar photovoltaic systems. Hence, under such a system, different local control parameters should be assured for the reliable and effective operation of a DC/AC microgrid. The DC to DC converter output voltage is automatically varied by wind MPPT and solar photovoltaic MPPT controller to the photovoltaic arrays and wind maximum-power-point-voltage (MPPV). The reference DC voltage

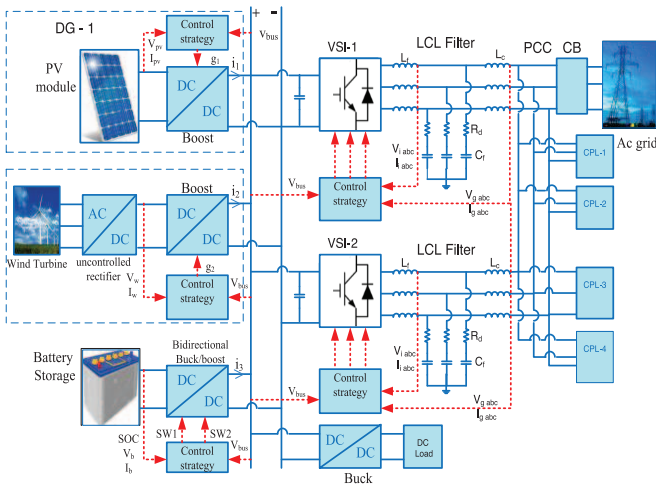


**Fig. 1.** Proposed hybrid DC/AC  $\mu$ G configuration.

setting to MPPV of wind, solar array, and reference current of a current-controlled inverter are analogous to the maximum extractable current from the source resulting in peak-power extraction from the renewable sources. A grid-connected hybrid DC–AC  $\mu$ G is primarily developed using the interlinking converters (ICs) as the crucial element for the bidirectional power transfer. The grid interlinking converter interfaces the DC-bus in DC  $\mu$ G to the AC bus in the AC primary grid; it aims to regulate constant DC voltage by inspecting the active power exchange among DC and AC systems. Two parallel ICs provide a modular function, plug-and-play features, fast dynamic response, and high reliability by incorporating frequency droop methods for appropriate load sharing among DERs in islanding mode. Hence, different local control parameters for a DC/AC microgrid are considered. The battery system operates on a standby, discharging, or charging mode. The photovoltaic (PV) and wind energy conversion (WEC) associated DC to DC converters employ MPPT. A DC to DC bidirectional converter is used with the battery to stabilize the grid power fluctuation and load variation. The grid voltage is tied to the current-controlled inverter output voltage, phase and frequency requirements are automatically met for synchronization.

The focal areas of this work are mentioned as follows:

1. Power quality is enhanced in both grid-interactive and islanding operations by a properly designed LCL filter with active damping by virtual droop control.
2. The virtual droop and MPPT control methods are used for parallel integration of renewable sources (solar, wind) connected to the DC-bus for current sharing involving multiple converters.
3. Dynamic power frequency droop control of parallel interlinking converters will share power in AC microgrid under load variation in islanded mode.
4. Adopting a decentralized control technique that eliminates dominance on faster communication in DC/AC microgrid control.

5. The hybrid system performance has been investigated under utility grid faults and input source fluctuations by the time domain simulation. The system recovers its steady state performance after fault clearing and it proves the rigidity of the decentralized control.
6. The realization of the islanding or grid-connected solar and wind generators associated with battery energy storage system ensure peak power management and flexibility of operation in islanding mode.

The paper is structured as follows. **Section 2** introduces the operation of a hybrid DC/AC microgrid. **Section 3** presents the control scheme of the DC/AC microgrid proposed. **Section 4** shows the simulation results and discussion. **Section 5** includes the experimental and HIL discussion. Finally, conclusions are indicated in **Section 6**.

## 2 Operation of hybrid DC/AC microgrid

The effective operation of multiple sources in DC/AC  $\mu$ G shall be accomplished with a decentralized control method considering both DC bus and AC bus signaling schemes. Such a control strategy catches an adaptive transition mode between the distinct operating modes. Hence, a bus voltage and frequency-based decentralized control is achieved to maintain the DC/AC  $\mu$ G system's applicable purpose for timely fluctuating input conditions.

**Table 1** shows the system's different modes of operation, such as injection in to the grid, distributed generation, and battery bank. The grid power flow ( $P_{\text{grid}}$ ) and the battery power ( $P_{\text{batt}}$ ) with the associated hybrid DC/AC  $\mu$ G types (grid-connected, autonomous) are mentioned.

The hybrid system of **Figure 1** and its various modes of operation are explained as follows:

### 2.1 Distributed generation mode

The DERs operation mode is shown in **Figure 2a**. The power at the grid is outaged; the system is shifted to autonomous mode. Because load demand is high, the DC-bus voltage decreases to the minimum limit in the operating range of  $1.025 V_{\text{dc}} < V_{\text{bus ref}} < 1.05 V_{\text{dc}}$ . The increased demand of load power is fulfilled by the wind-PV subsystem and batteries.

### 2.2 Grid-injection mode

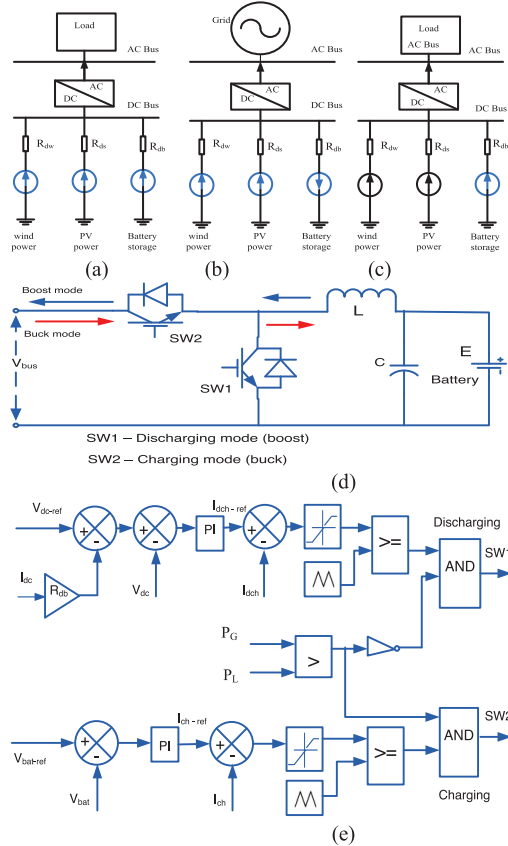
The excess power generation from DERs is exported to the grid. In this operation, the storage is charging, the ICs are considered current sources, and the generation mode is indicated in **Figure 2b**. **Figure 3a** shows that the interlinking converter's control is performed by measuring the DC subgrid voltage and applying the PLL to catch the frequency and AC voltage amplitude.

### 2.3 Battery energy storage mode

As depicted in **Figure 2c**, distributed generation (DG) is under short maintenance in this operating mode.

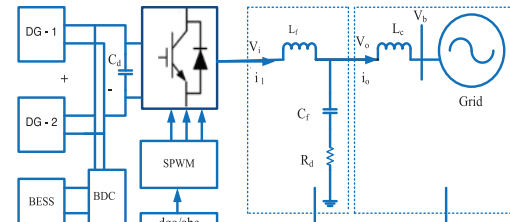
**Table 1.** System operating modes.

Operating modes	DC/AC $\mu$ G type	Power flow
DG	Islanding	$P_{\text{grid}} = 0, P_{\text{batt}} > 0$
Grid injection	Grid-connected	$P_{\text{grid}} > 0, P_{\text{batt}} < 0$
BESS	Islanding	$P_{\text{grid}} = 0, P_{\text{batt}} > 0$

**Fig. 2.** DG operating modes and proposed control of energy storage: (a) DG mode, (b) grid-injection, (c) BESS mode, (d) bidirectional battery converter (BDC) and (e) proposed BDC control.

The primary grid is turned off, and the battery bank provides emergency loads.

Figure 2d shows the bi-directional DC–DC buck/boost power circuit diagram at the DC link. For buck mode of operations, the DC bus voltage ( $V_{\text{bus}}$ ) is greater than the typical battery voltage ( $E$ ). Two proportional integral controllers regulate the DC voltage at the buck-boost converter's desired value. Figure 2e indicates a battery-suggested control strategy, the reference bus voltage ( $V_{\text{dc-ref}}$ ) compared to the operating voltage ( $V_{\text{dc}}$ ), and the PI controller executes the error signal. The controller output signal is fed to the SW1, and SW2 switches duty cycle according to a state of discharging or charging. The discharging process (SW1 on) only occurs when load power ( $P_L$ ) is higher than the generation ( $P_G$ ); charging occurs only when  $P_G$  is greater than  $P_L$  (SW2 on). When  $P_G = P_L$ , both switches are turned off so that battery is neither charging nor discharging.

**Fig. 3.** Proposed control scheme: (a) proposed grid-connected P/Q control, (b) proposed control of solar PV system using constant voltage control and MPPT control method and (c) proposed PMSG constant voltage control and MPPT control method.

The buck operation is correlated with charging, and the boost function is in discharging mode. The reference battery voltage ( $V_{\text{bat-ref}}$ ) is compared with the operating voltage ( $V_{\text{bat}}$ ), and then the error is processed through the PI controller. The controller provides a reference battery charging current ( $I_{\text{ch-ref}}$ ) compared to the actual battery charging current ( $I_{\text{ch}}$ ). The error current after the saturation block is again compared with a triangular pulse; this provides a necessary gate pulse for buck mode. Similarly, the discharging current ( $I_{\text{d ch-ref}}$ ) is measured against the actual ( $I_{\text{d ch}}$ ) battery discharging current, and then the error is passed through the saturation block, compared to a triangular wave to produce gate pulses in the boost mode.

### 3 Control of proposed DC/AC microgrid

#### 3.1 Grid-connected converter (GCC) control

Figure 3a shows DGs and battery control with the grid through the voltage source inverter under a dynamic reactive and active power control scheme. In this architecture, the subsequent controller used for desirable dynamic performance, such as phase detector, inverter output voltage sensor, current detector, instantaneous power ( $P/Q$ ) computation, power PI controller, Park-transformation (dqo to abc, and vice-versa), current PI controller, and sine pulse width modulation (SPWM). The synchronously rotating control strategy can be implemented in the  $d-q$  frame reference [26]. A feedback control parameter of the inverter and grid side current and voltage estimates the instantaneous power ( $P/Q$ ) and ensures a tight inner current control loop.

In the  $d-q$  frame, the instantaneous reactive and real power can be calculated by:

$$p = \frac{3}{2}(v_d i_d + v_q i_q), \quad (1)$$

$$q = \frac{3}{2}(v_d i_q - v_q i_d), \quad (2)$$

where  $q$  is reactive power, and  $p$  is active power. Frequency and voltage output references are estimated as:

$$V_{od\text{ref}} = V_{\text{ref}} - n_q Q, \quad V_{oq\text{ref}} = 0, \quad (3)$$

$$\omega = \omega_{\text{ref}} - m_p P, \quad (4)$$

where  $n_q$  and  $m_p$  are the droop coefficients.

#### 3.2 Control of PV array using MPP tracking

The input irradiance of solar photovoltaic is changing; to gather maximum solar array power, MPPT is engaged in the proposed topology. The variable module output DC-voltage provided to the solar converter is demonstrated in Figure 3b. The solar boost converter achieves maximum power tracking and facilitates the full power capture of DERs during a change in ambient conditions. In this paper, using perturbation and observation (P&O) application for tracking, MPPT is implemented [27]. The proposed constant voltage and MPPT control of the solar energy is shown in Figure 3b.

#### 3.3 PMSG wind system MPP tracking

The input wind velocity of the PMSG wind turbine varies. Due to changing speed of the wind, the maximum power obtained from PMSG with MPPT accommodates the demand. This power is shared in the common DC-bus and among parallel ICs interfacing with the DGs. The wind system produces AC three-phase voltage. The uncontrolled rectifier changes variable AC voltage to DC voltage; the voltage outputs feed the DC-DC boost converter to track the MPPT. The proposed constant voltage and MPPT control of the wind is demonstrated in Figure 3c.

The mechanical power obtained from the wind system ( $P_m$ ), torque coefficient ( $C_q$ ), tip-speed ( $\lambda$ ), and the turbine torque ( $T_m$ ) is determined by (5)–(8).

$$P_m = \frac{1}{2} \rho A C_p (\beta, \lambda) V_{\text{wind}}^3, \quad (5)$$

$$C_q = \frac{C_p}{\lambda}, \quad (6)$$

$$\lambda = \frac{R\omega}{V_{\text{wind}}}, \quad (7)$$

$$T_m = \frac{P_m}{\omega} = \frac{1}{2} \rho \pi C_q R^3 V_{\text{wind}}^2, \quad (8)$$

where  $C_p$  – power coefficient,  $\rho$  – air density ( $\text{kg/m}^3$ ),  $\beta$  – blade pitch angle (radian),  $V_{\text{wind}}$  – wind speed ( $\text{m/s}$ ),  $A$  – turbine area ( $\text{m}^2$ ),  $R$  – radius of the turbine blade (m),  $\omega$  – turbine rotational angular frequency (rad/sec).

#### 3.4 Islanding microgrid control

The circuit breaker (CB) is indicated in Figure 1. If the CB is kept open, the microgrid is intended for islanded or autonomous operation. The microgrid should maintain its frequency and voltage as the primary grid in this situation. Figure 4 shows the proposed controllers such as voltage control, power with droop control, and current control during a smooth changeover from grid-tied to standalone mode. In islanding mode, the voltage controller depicted in Figure 4b produces current reference values for the current controller. Figure 4a shows power control incorporated droop characteristics for load sharing, used to generate reference voltage values and the angle required for park transformation (abc to dqo conversion) and vice-versa. The current controller shown in Figure 4c generates reference voltages used in SPWM and makes the desired current system meet the load.

The power controller schematic is described in Figure 4a. The synchronous generators in traditional power systems share the load increment according to governor droop characteristics by decreasing frequency. This concept is implemented in the inverter by reducing the frequency reference while increasing load. Correspondingly, the reactive power can be shared by announcing droop characteristics in voltage amplitude. Figure 4a shows the instantaneous reactive-power ( $q$ ) and real power ( $p$ ) components that are computed using the measured output currents and voltages by (1) and (2). The instantaneous power is processed through the low pass filter (LPF) shown in (9) to get real ( $P$ ) and reactive ( $Q$ ) power at the fundamental frequency.  $\omega_c$  is the LPF cutoff frequency.

$$P = \frac{\omega_c}{S + \omega_c} p, \quad Q = \frac{\omega_c}{S + \omega_c} q. \quad (9)$$

The power distribution among parallel ICs is done by incorporating a droop in the IC shown in (10a)–(10c). The IC voltage angle  $\alpha$  varies in feedback to power ( $P$ ) flow in the suitable gloomy sight, and gain addressed by droop is given in (10d) and (10e).

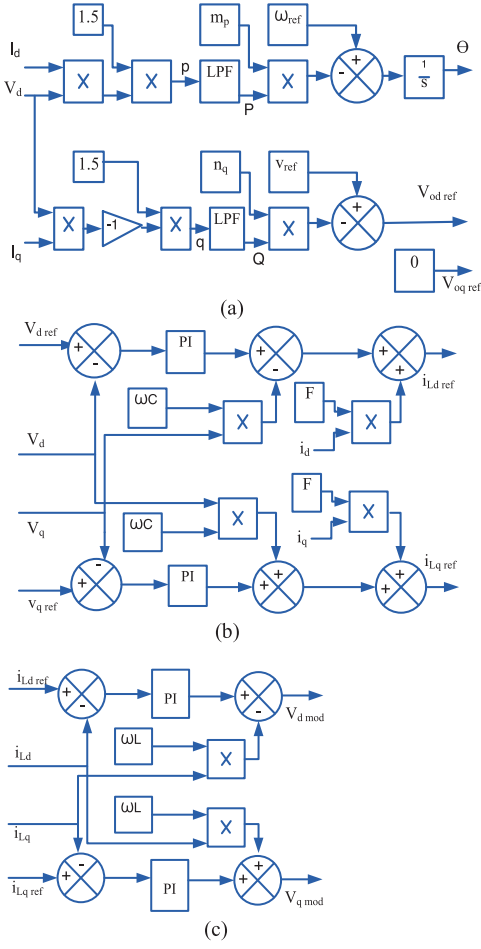


**Fig. 4.** Proposed autonomous mode control: (a) power with droop control, (b) voltage control and (c) current control.

$$\omega = \omega_{ref} - m_p P, \quad (10a)$$

$$\dot{\theta} = \omega, \quad (10b)$$

$$\theta = \omega_{ref} t - \int m_p P dt, \quad (10c)$$

$$\alpha = - \int m_p P dt, \quad (10d)$$

$$\dot{\alpha} = - m_p P. \quad (10e)$$

The voltage controller block diagram is shown in Figure 4b, consisting of all feed-forward ( $F$ ) and feedback terms. The corresponding equations are written in (11) and (12).

$$\begin{aligned} i_{Ld\ ref} &= Fi_d - \omega CV_q + k_{pdv} (V_{d\ ref} - V_d) + k_{idv} \\ &\times \int (V_{d\ ref} - V_d) dt, \end{aligned} \quad (11)$$

$$\begin{aligned} i_{Lq\ ref} &= Fi_q + \omega CV_d + k_{pqv} (V_{q\ ref} - V_q) + k_{iqv} \\ &\times \int (V_{q\ ref} - V_q) dt, \end{aligned} \quad (12)$$

where  $i_{Ld\ ref}$  – direct-axis filter inductor reference current component, and  $i_{Lq\ ref}$  – quadrature-axis filter inductor reference current.

Figure 4c shows the current controller structure. The standard PI controllers provide the control of the filters inductor current; the corresponding algebraic equations are given in (13) and (14).

$$V_{d\ mod} = -\omega Li_{Lq} + k_{pdc} (i_{Ld\ ref} - i_{Ld}) + k_{idc} \int (i_{Ld\ ref} - i_{Ld}) dt \quad (13)$$

$$V_{q\ mod} = \omega Li_{Ld} + k_{pqc} (i_{Lq\ ref} - i_{Lq}) + k_{iqc} \int (i_{Lq\ ref} - i_{Lq}) dt \quad (14)$$

where  $V_{d\ mod}$ ,  $V_{q\ mod}$  – are the components referring to direct-axis and quadrature-axis inverter voltages reference, respectively.

### 3.5 Source converter droop analysis

A droop method will enable distributed renewable sources to operate in parallel to share loads in line with generation capacities [28]. The circulating current problem among parallel-connected converters has been mitigated by the active damping of the most dominating power source. For example, the active rectifier introduces active damping in a grid-connected mode. Furthermore, droop with MPPT control is engaged in attaining the current sharing between parallel converters. Droop control adds feedback current to a voltage-current inner loop of wind and solar PV units, which is synthetically developing output impedance for individual converters, as depicted in Figures 3b and 3c. The equivalent voltage of DGs ( $V_n$ ) associated with a series droop ( $R_d$ ) making the reference voltage ( $V_{bus\ ref}$ ) can be determined by [29], as shown in (15) below:

$$V_{bus\ ref} = V_n - R_d i_o, \quad (15)$$

$i_o$  is output current.

The droop value ( $R_d$ ) connected at each source is calculated using (16).

$$R_d = \frac{\Delta v_{bus}}{i_{max}}. \quad (16)$$

$\Delta v_{bus}$ ,  $i_{max}$  are maximum voltage deviation and maximum current for interface converter, respectively.

The terminal current ( $i_s$ ) at each converter shown in Figure 1 is

$$i_s = i_1 + i_2 + i_3, \quad (17)$$

where  $i_1$ ,  $i_2$ , and  $i_3$  are the solar, wind, and battery currents, respectively.

Considering the same source voltage under consistent voltage control, the bus reference voltage is computed in (18).

$$V_{bus\ ref} = V_n - \frac{1}{\sum_{i=1}^n \frac{1}{R_{di}}} i_s = V_n - R_d i_s. \quad (18)$$

Each DG in the AC subgrid has a converter empowered from renewable DC sources [30]. The DGs can supply the load according to the droop gain [31]. The summation of all active injected power of DGs should equal the AC loads shown in (19a).

$$P_{\text{ac load}} = \sum_{i=1}^n P_{\text{ac}}(i) \cdot m_{\text{ac}}(i), \quad (19\text{a})$$

where  $P_{\text{ac load}}$  – total AC load power,  $m_{\text{ac}}(i)$  – generation droop gain,  $P_{\text{ac}}(i)$  – each DG supplied power, and  $n$  gives the number of generation. The DC-bus voltage is managed using droop control in the DC subgrid. All injected power to the DC grid equals all DC loads seen in (19b).

$$P_{\text{dc load}} = \sum_{k=1}^n P_{\text{dc}}(i) \cdot m_{\text{dc}}(i), \quad (19\text{b})$$

where  $P_{\text{dc}}(i)$  – DG injected power and  $m_{\text{dc}}(i)$  – a gain of each generation.

### 3.6 LCL filter modeling

The single-phase circuit schematic of the LCL filter is described in Figure 5a. Where  $i_s$ ,  $i_c$ ,  $L_f$ ,  $L_c$  represent the grid side current, converter current, filter inductance, and converter side inductance, respectively. Accordingly, the state-space equation is written in (20)–(22).

$$\frac{dv_{cf}}{dt} = \frac{1}{C_f}(i_s - i_c), \quad (20)$$

$$\frac{di_s}{dt} = \frac{1}{L_f}(v_s - R_d(i_s - i_c) - v_{cf}), \quad (21)$$

$$\frac{di_c}{dt} = \frac{1}{L_c}(v_{cf} + R_d(i_s - i_c) - v_{\text{conv}}). \quad (22)$$

Representing in state-space form as expressed in (23).

$$\begin{bmatrix} \frac{di_c}{dt} \\ \frac{di_s}{dt} \\ \frac{dv_{cf}}{dt} \end{bmatrix} = \begin{bmatrix} -\frac{R_d}{L_c} & \frac{R_d}{L_c} & \frac{1}{L_c} \\ \frac{R_d}{L_f} & -\frac{R_d}{L_f} & -\frac{1}{L_f} \\ -\frac{1}{C_f} & \frac{1}{C_f} & 0 \end{bmatrix} \begin{bmatrix} i_c \\ i_s \\ v_{cf} \end{bmatrix} + \begin{bmatrix} -\frac{1}{L_c} & 0 \\ 0 & \frac{1}{L_f} \\ 0 & 0 \end{bmatrix} \begin{bmatrix} v_{\text{conv}} \\ v_s \end{bmatrix}. \quad (23)$$

The filter transfer function is expressed in (24).

$$G_{\text{LCL}}(s) = \frac{C_f R_d s + 1}{(L_f C_f L_c) s^3 + C_f (L_f + L_c) R_d s^2 + (L_f + L_c) s}. \quad (24)$$

For filter design, the inverter inductor ( $L_f$ ), filter capacitor ( $C_f$ ), grid inductor ( $L_c$ ), resonant frequency ( $\omega_{\text{res}}$ ) and passive damping ( $R_d$ ) are given by (25)–(29).

$$L_f = \frac{V_{DC}}{6 f_{\text{sw}} \Delta I_{L_{\max}}}, \quad (25)$$

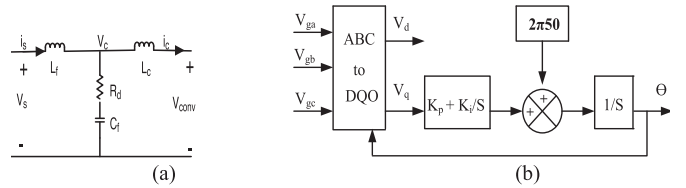


**Fig. 5.** Single-phase LCL filter and three-phase synchronous reference frame (a) LCL filter circuit diagram and (b) PLL.

$$L_c = \sqrt{\frac{1}{k^2} + 1} \frac{1}{C_f \omega_{\text{sw}}^2}, \quad (26)$$

$$C_f = \frac{0.01}{0.05 C_b}, \quad (27)$$

$$\omega_{\text{res}} = \sqrt{\frac{L_f + L_c}{L_f L_c C_f}}, \quad (28)$$

$$R_d = \frac{1}{3 \omega_{\text{res}} C_f}, \quad (29)$$

where  $V_{\text{DC}}$  – DC-link voltage,  $f_{\text{sw}}$  – switching frequency,  $k$  – desired attenuation, and  $C_b$  – the base capacitance.

### 3.7 Maximum power point tracking

The power generation from DERs varies as input wind speed and solar irradiance vary. Figure 3b shows the MPPT employed in solar PV systems. Figure 3c shows the MPPT configured for the wind system. MPPT aims to use a control algorithm to assure PV arrays and wind generators to operate at maximum power point under input variations. Selman and Mahmood [32] describe the different power tracking algorithms like incremental-conductance, perturb & observe (P&O), neural networks, pilot cell, and fuzzy logic (FL). The classification of MPPT techniques rely on features: control variables required, cost, number of sensors, and speed of implementation. In this paper, the P&O technique used due to low computational demand requires solar voltage, solar current, wind voltage, and wind current for better performance.

### 3.8 Phase-locked loop (PLL)

The grid synchronization performs essential functions for grid-interactive systems. Figure 5b shows the PLL operating in synchronous reference frame (SRF). The three-phase SRF PLL subsisting of three components are the loop filter (LF), a phase detector (PD), and a phase/frequency generator, also known as a voltage-controlled oscillator. The synchronously rotating control strategy can be carried out within the  $d$ - $q$  frame references in grid synchronization. The direct-quadrature ( $d$ - $q$ ) PLL is developed according to the Park's and Clarke's transformation indicated in (30), which converts the abc stationary frame into  $d$ - $q$  synchronous frame.

$$\begin{bmatrix} V_d \\ V_q \end{bmatrix} = \frac{2}{3} \begin{bmatrix} \cos(\theta) & \cos(\theta - 120) & \cos(\theta + 120) \\ -\sin(\theta) & -\sin(\theta - 120) & \sin(\theta + 120) \end{bmatrix} \begin{bmatrix} V_a \\ V_b \\ V_c \end{bmatrix}. \quad (30)$$

The SRF phase-locked-loop uses abc-dq transformation block; the phase-detector converts the positive sequence utility phase voltage (31) to the quadrature ( $q$ ) channel signal.

$$\begin{bmatrix} V_{ga} \\ V_{gb} \\ V_{gc} \end{bmatrix} = \begin{bmatrix} V_g \cos(\theta) \\ V_g \cos\left(\theta - \frac{2}{3}\pi\right) \\ V_g \cos\left(\theta + \frac{2}{3}\pi\right) \end{bmatrix}. \quad (31)$$

### 3.9 Stability analysis

The microgrid's entire system dynamics depend on the associated components; the frequency domain method has been employed to examine the system stability analysis.

In a physical system, the load interface converters can inject pulsating currents into a power network. The injected current comprises of high order harmonics, which affect the current spike coming from the switching transition. To overcome such problems, an input filter is engaged at the converter's terminal. This filter with optimum damping can stabilize the system, as illustrated in Figure 6a. The optimum resistance ( $R_{d1}$ ) for damping can be estimated considering the peak output impedance of the filter ( $Z_o$ ), as written in (32).

$$Z_{o \max} = R_o \frac{\sqrt{2(2+n)}}{n}, \quad (32)$$

where  $R_o = \sqrt{\frac{L_f}{C_f}}$  and  $n = \frac{C_d}{C_f}$ . The damping resistor ( $R_{d1}$ ) can be determined in (33).

$$R_{d1} = R_o \sqrt{\frac{(2+n)(4+3n)}{2n^2(4+n)}}. \quad (33)$$

The buck DC-DC converter with dc load side input filter and its voltage control is indicated in Figures 6a and 6b, respectively. The load converter open-loop control transfer function ( $G_{vd}(s)$ ) with damped filter is expressed as in (34).

$$G_{vd}(s) = V_g \frac{a_3 s^3 + a_2 s^2 + a_1 s + 1}{b_5 s^5 + b_4 s^4 + b_3 s^3 + b_2 s^2 + b_1 s + b_0}, \quad (34)$$

where denominator and numerator are given as,

$$a_1 = n C_f R_{d1} - D^2 L_f / R,$$

$$a_2 = L_f C_f \left(1 + n - \frac{n D^2 L_f}{R}\right), \quad a_3 = n L_f C_f^2 R_{d1},$$

$$b_0 = 1, \quad b_1 = n C_f R_{d1} + (L + D^2 L_f) / R,$$

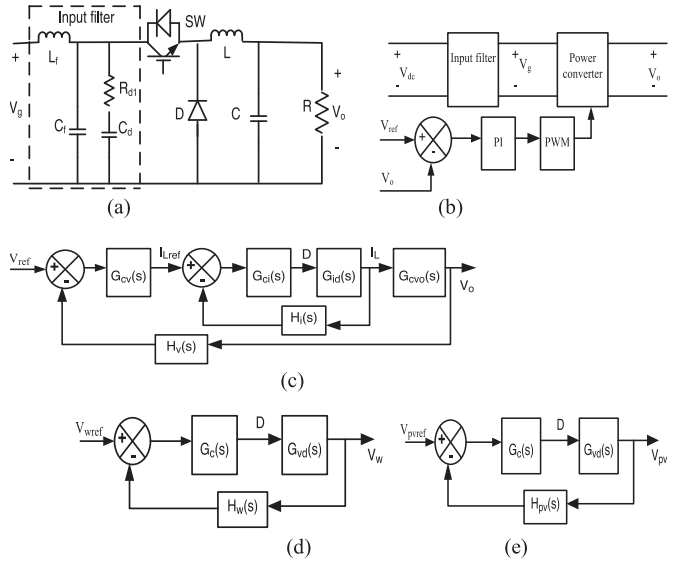


**Fig. 6.** Buck converter and controller transfer function block diagram: (a) buck converter topology, (b) control block diagram of buck converter, (c) solar and wind boost converter controller block diagram, (d) wind control in MPPT mode and (e) solar control in MPPT mode.

$$b_2 = C(D^2 L_f + L) + L_f C_f + n L_f C_f + n C_f R_{d1} (L + D^2 L_f) R,$$

$$b_3 = \frac{L_f C_f L (1+n)}{R} + n C_f R_{d1} (L_f C_f + LC + D^2 L_f C),$$

$$b_4 = L_f C_f L (1+n) + n L_f L R_{d1} C_f^2 / R,$$

$$b_5 = n L_f C_f^2 L C R_{d1}.$$

#### 3.9.1 Controller transfer function

The controller block diagram of solar and wind in controlled voltage mode and MPPT control mode is depicted in Figures 6c–6e.

The average state-space equation of boost converter is expressed as (35) and (36).

$$L \frac{\delta \Delta i_L(t)}{\delta t} = \Delta V_{in}(t) - (1-\delta) \Delta V_c(t) + V_c \Delta \delta(t), \quad (35)$$

$$C \frac{\delta \Delta V_c(t)}{\delta t} = (1-\delta) \Delta i_L(t) - i_L \Delta \delta(t) - \frac{1}{R} \times \Delta V_c(t), \quad (36)$$

where  $\delta$ ,  $L$ ,  $i_L$ ,  $V_{in}$ ,  $C$ ,  $V_c$ ,  $R$  are the duty cycle, inductor, inductor current, input voltage, capacitor, capacitor voltage, and load resistance of the boost converter, respectively.

Transforming (35) and (36) into the frequency domain and simplifying the equation, the converter control to output voltage transfer function, control to inductor current

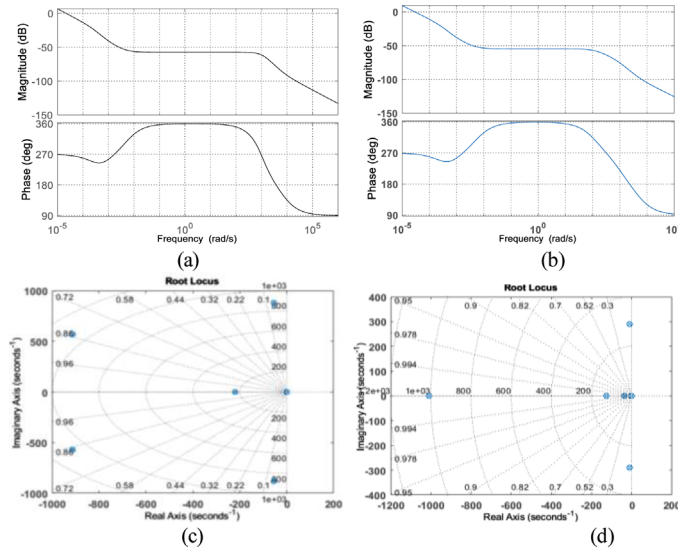


**Fig. 7.** Frequency response and root locus (a) frequency response of wind converter (voltage open-loop gain), (b) frequency response of solar converter (voltage open-loop gain), (c) root locus of wind converter (voltage closed-loop) and (d) root locus of solar converter (voltage closed-loop).

transfer function, and inductor current to output voltage transfer function are obtained in (37)–(39).

$$G_{vd}(s) = \frac{\Delta V_o(s)}{\Delta \delta(s)} = \frac{(1-\delta)V_o - (LI_L)s}{(LC)s^2 + \frac{L}{R}s + (1-\delta)^2}, \quad (37)$$

$$G_{id}(s) = \frac{\Delta i_L(s)}{\Delta \delta(s)} = \frac{CV_o s + 2(1-\delta)I_L}{(LC)s^2 + \frac{L}{R}s + (1-\delta)^2}, \quad (38)$$

$$G_{iv}(s) = \frac{\Delta V_o(s)}{\Delta i_L(s)} = \frac{(1-\delta)V_o - (LI_L)s}{(CV_o)s + 2(1-\delta)I_L}, \quad (39)$$

where  $V_o$  is the boost converter output voltage.

In the case of MPPT control, the converter loop gain is achieved by multiplying the plant transfer function and controller in the frequency domain, as shown in (40).

$$G_{voL}(s) = G_c(s) * G_{vd}(s), \quad (40)$$

where  $G_c(s)$  is the PI controller transfer function. Similarly, the open-loop voltage and the current transfer function are given in (41) and (42).

$$G_{ioL}(s) = G_{ci}(s) G_{id}(s), \quad (41)$$

$$G_{voL}(s) = G_{cv}(s) G_{cl}(s) G_{cvo}(s), \quad (42)$$

where  $G_{cl}(s) = \frac{G_{ci}(s) G_{id}(s)}{1 + G_{ci}(s) G_{id}(s)}$ .

PI controller gain is selected from the bode plot. The gain and phase margin are chosen so that the system is stable and a fast dynamic response is ensured. It is demonstrated in Figure 8e for dynamic change in load and fault conditions simulated are shown in Figures 11a–11c.

Figures 7a–7d show the frequency response and root locus of the wind and solar voltage loop. The solar operates

at a gain margin of 2.1539e+04 and a phase margin of 86.5736. The wind system operates at a phase margin of 87.3661 and a gain margin of 8.1979e+03.

## 4 Results of simulation and discussion

The proposed topology with the decentralized control has been simulated in the MATLAB/Simulink environment to validate the simulation outcomes.

### Case 1: Solar irradiation and wind speed variations.

The DERs input source variations (solar irradiation, wind speed) are revealed in Figures 8a and 8b. Figure 8a shows the solar irradiance from 0 to 2 s, 2 to 5 sec, and 5 to 7 sec is 700 W/m<sup>2</sup>, 1000 W/m<sup>2</sup>, and 700 W/m<sup>2</sup>, respectively. The peak power generated is 3 kW during this solar variation, as indicated in Figure 9a. As shown in Figure 8b, the wind speed from 0 to 2 s, 2 to 5 s, and 5 to 7 s is 10.8 m/s, 12 m/s, and 10.8 m/s, respectively. In this wind speed fluctuation, peak power generation is 6.5 kW, as shown in Figure 9c. Thus, the controller tracks the optimum power according to the source variations of solar irradiation, and wind speed confirms the proposed controller's effectiveness.

Figure 8c displays the three-phase voltage outputs waveform of the inverter during the islanding operating mode. Figure 8d depicts the inverter pole voltages. Figure 8e indicates the output waveform change of the three-phase load current due to a change in load. Figure 8f shows the droop angle ( $\theta$ ) of the parallel ICs controller operating in the autonomous mode. The angle obtained from power droop control is required for three-phase voltages and currents transformation (abc-dqo-abc) in islanding operation. Figure 9a shows 3 kW peak power generation from solar PV, and Figure 9c shows the generation of 6.5 kW of the

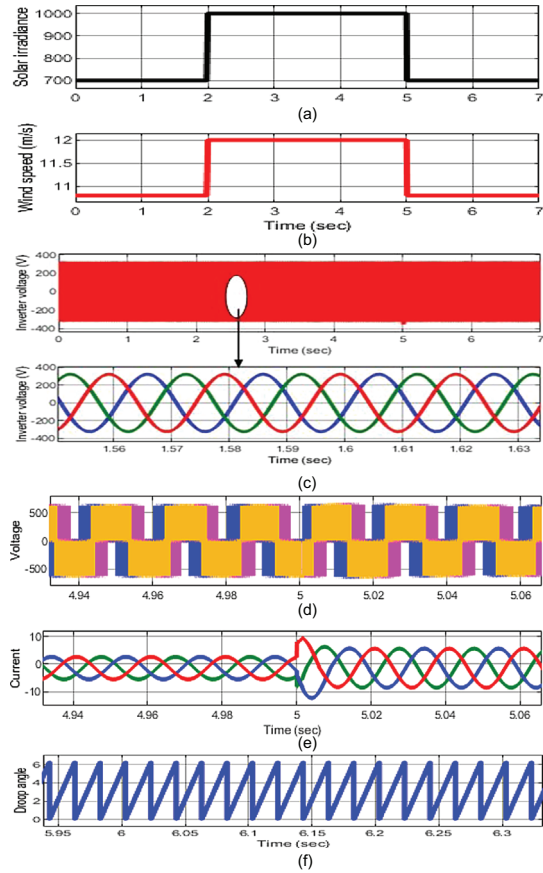


**Fig. 8.** DERs input variation and islanding waveform output: (a) solar irradiation fluctuations ( $\text{W}/\text{m}^2$ ), (b) variable wind speed ( $\text{m}/\text{s}$ ), (c) waveform inverter (VSI-1) output voltage after the filter, (d) three-phase inverter voltages (V), (e) step load change current and (f) parallel ICs droop angle.

wind system. Figure 9d shows grid line voltage and islanding line voltage at PCC, having the same voltage amplitude, phase sequence, and angle. Thus, it demonstrates the efficacy of the proposed control system.

#### Case 2: Variation of the loads.

Distributed generations and BESS are activated at a time ( $t$ ) = 0 s permitted to achieve steady-state, and all DGs are connected at PCC. At  $t$  = 0 s, a load of 2 kW near DG-1 and load-3 of 2 kW near DG-2 is turned on. At  $t$  = 5 s, a load of 3.5 kW near DG-1 is turned on. Another load-4 of 3.5 kW near DG-2 is switched on, and the corresponding demand is shown in Figures 9e and 9f. Figure 8c shows that the simulation output of three-phase voltages for both ICs is synchronous with the essential value even through load changes instantaneously. The simulation result of three-phase currents, which depends on output voltages and load adjustment at five seconds, is illustrated in Figure 8e. A step change of load is initiated at five seconds, and the controller ensures that the transient is mitigated within one cycle. Both loads shared depend on the droop coefficients in the steady-state condition, and the current shared also depends on droop coefficients. The power of the load demand is indicated in Figures 9e and 9f.

Figures 9g and 9h show the fast Fourier transform of inverter current and voltage, respectively. The inverter voltages after the LCL filter, the total harmonic distortion (THD) obtained is 0.78%, and the current output THD is 0.67% compared to [26] of current THD 3.68% and [23] voltage THD 4.12%. The lower current and voltage THD value demonstrate that controllers work efficiently, and the overall structure of the designed DC/AC microgrid is at optimum. Furthermore, the system's efficacy may be observed in the transient system stability by the droop control methods proposed. However, it was reported to be a drawback [33].

#### Case 3: Charging and discharging of BESSs.

The BESS bank power shown in Figure 9j is necessary to fulfill the load demands in Figures 9e and 9f. During 0–2 s, 2 kW power is produced by PV, and 3 kW wind power is generated, as demonstrated in Figures 9a and 9c, respectively. The sum of load-1 and load-3 is 4 kW, which is lower than all DERs' power, as indicated in Figures 9e and 9f. At this time, DC/AC μG is in islanding, and all DERs generation can provide load demand. As shown in Figure 9a, from 2 to 5 s, solar PV generation is 3 kW, and wind power is 6.5 kW shown in Figure 9c; at this time, the total demand is 4 kW. There is 5.5 kW of extra power produced during this period; the BESSs are charging, as shown in Figure 9j. From 5.01 to 7 s, solar PV generation is reduced to 2 kW, and wind generation is 3 kW. However, load-2 has a 3.5 kW power demand, and load-4 requires 3.5 kW power. In such circumstances, total DERs power comes out to be 5 kW and thus cannot supply a whole load of 7 kW. Therefore, the extra 2 kW load demand can be provided from BESSs in discharging mode, as shown in Figure 9j.

#### Case 4: Fault conditions and input source disturbance.

The 3-phase line to line (LLL) fault is introduced at the PCC in the system at  $t$  = 5.05 to 5.1 s. During this period, the three-phase currents increase, and three-phase voltages are zero. After clearing the fault, at  $t$  = 5.1 s, the controller quickly keeps the system moving towards steady-state operation and maintains the system voltage control and power balance. During fault conditions, Figures 11a–11c show the output inverter voltages (before filter), inverter voltages (after the filter), and load currents, respectively.

The variable wind velocity and solar irradiation are the input disturbances provided to the system, as indicated in Figures 10a and 10b. The controller tracks the optimum power according to the source variations of solar irradiation, and wind speed confirms the adequate performance of the proposed controllers. Figures 10a and 10c show the variation of solar irradiance ( $\text{W}/\text{m}^2$ ) and the associated output power, respectively. At 0–1 s, the irradiance is 800  $\text{W}/\text{m}^2$ , and the power output is 2000 W. From 1 to 6 s, the irradiance rises to 1000  $\text{W}/\text{m}^2$ , and the corresponding power output is 3000 W. In 6–7 s, irradiance decreases to 800  $\text{W}/\text{m}^2$ ; its output power is also reduced to 2000 W. Figures 10b and 10c indicate the wind velocity variation and the power output, respectively. At a low wind speed of 11.28 m/s and the highest wind speed of 12.24 m/s,

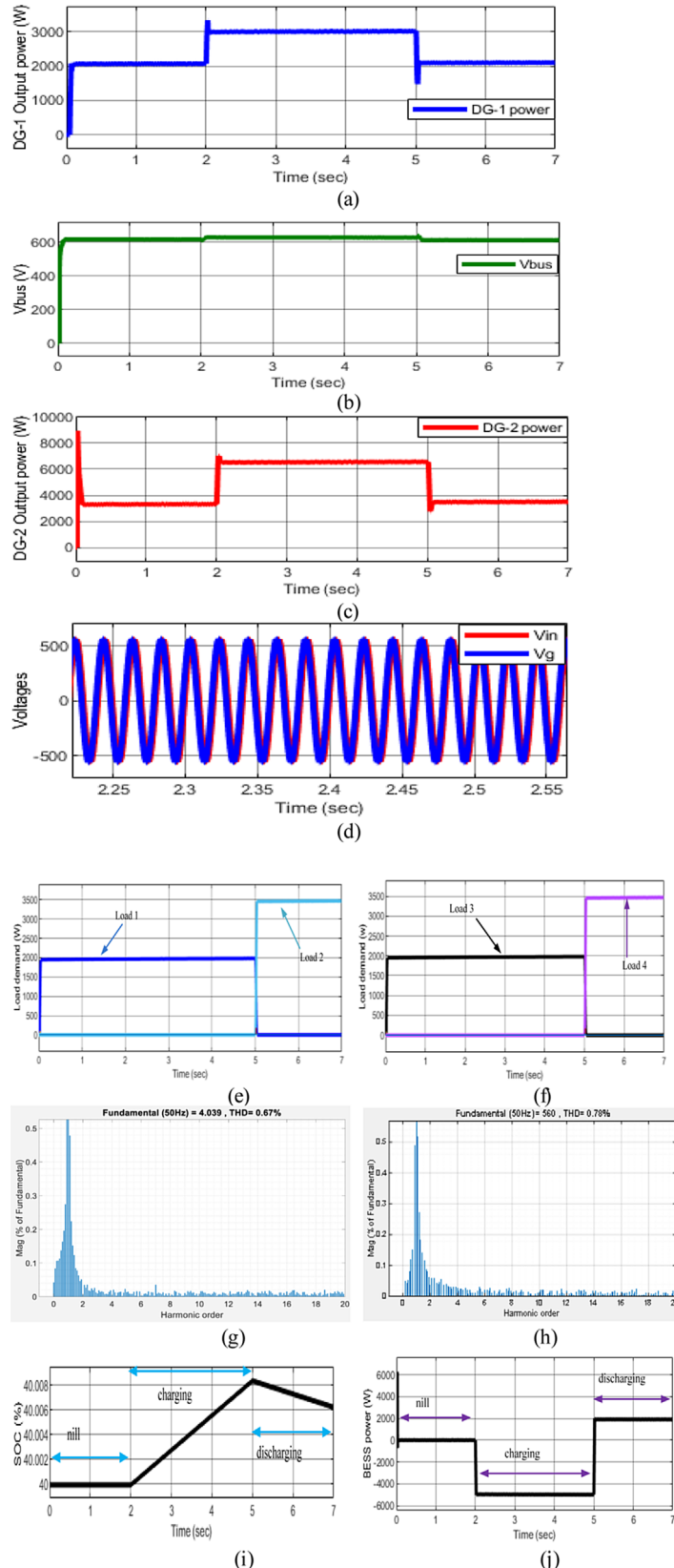


**Fig. 9.** Power output waveforms: (a) DG-1 output power, (b) DC-link voltage, (c) DG-2 output power, (d) grid voltage ( $V_g$ ) and inverter line voltage ( $V_{in}$ ), (e) power demand near DG-1, (f) demand power near DG-2, (g) the inverter current THD (after the filter), (h) inverter line voltage THD estimations, (i) BESS SOC and (j) Battery power (W) when charging/discharging.

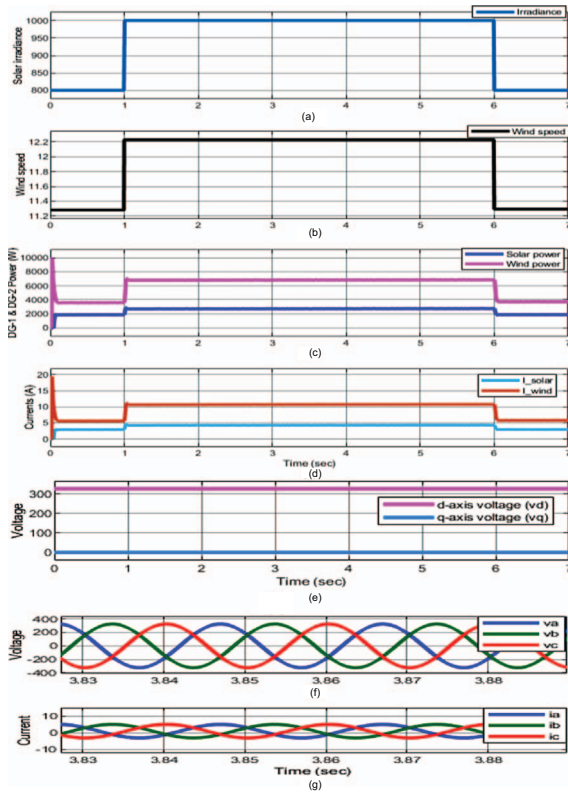


**Fig. 10.** Outputs: (a) solar irradiation ( $\text{W}/\text{m}^2$ ), (b) wind velocity ( $\text{m}/\text{s}$ ), (c) solar output power (W) (DG-1) and wind output power (W) (DG-2), (d) solar output current (A) and wind output current (A), (e) direct and quadrature axis voltage (V), (f) inverter (VSI-2) output voltage (V) after the filter and (g) load current (A) (VSI-2).

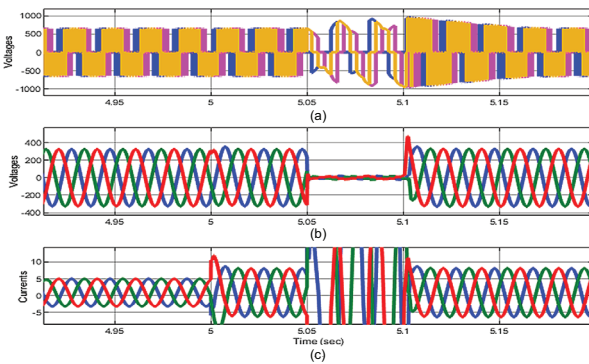


**Fig. 11.** Fault condition: (a) the inverter voltage (before the filter), (b) the inverter voltage (after the filter) and (c) load current.

the generation capacity is 3800 W and 6500 W, respectively. Figures 10e–10g present the voltage source inverter (VSI-2) output direct axis voltage, quadrature voltage, three-phase voltage, and load current, respectively.

Table 2 indicates the design variables used for the model proposed. Table 3 provides the controller parameters of the studied system.

**Table 2.** System design parameters.

Units	Parameters	Values
Solar	Rated power	3 kW
	PV module voltage	240 V
	Switching-frequency	8 kHz
Wind	Rated power	6.5 kW
	Wind output voltage	400 V
	Switching frequency	8 kHz
BESS	Rated capacity	200 Ah
	Switching frequency	8 kHz
Filter	Inductor ( $L_f$ )	22.26 mH
	Inductor ( $L_c$ )	0.79 mH
	Filter ( $C_f$ )	50 $\mu\text{F}$
	Damping resistor ( $R_d$ )	5.3 $\Omega$
Load-1	Power	2 kW
Load-2	Power	3.5 kW
Load-3	Power	2 kW
Load-4	Power	3.5 kW
Grid	Voltage	400 V
	Power	5 kW

**Table 3.** Proposed system controller parameters.

Units	Parameters	Symbols	Values
Interlinking converter	Voltage control loop	$k_{PV}$	5
	Current control loop	$k_{iv}$	0.0005
	Voltage control loop	$k_{pv}$	0.04
	Current control loop	$k_{ic}$	0.01
Solar boost converter	Voltage control loop	$k_{PV}$	0.000190
	Current control loop	$k_{iv}$	0.0002018
	Voltage control loop	$k_{pv}$	0.0111
	Current control loop	$k_{ic}$	7.2
Wind boost converter	Voltage control loop	$k_{PV}$	25
	Current control loop	$k_{iv}$	10
	Voltage control loop	$k_{pv}$	0.0503
	Current control loop	$k_{ic}$	48.1
BESS converter	Voltage control loop	$k_{PV}$	0.089
	Current control loop	$k_{iv}$	245
	Voltage control loop	$k_{pv}$	0.0177
	Current control loop	$k_{ic}$	10

## 5 Experimental results and HIL

The experimental prototype is made using a battery bank, LCL filter, Semikron IGBT switches, CPL and controlled by dSPACE-1104 (Figure 12).

The real-time simulation is essential to justify the controller's accuracy and performance; hence the developed model in OPAL-RT is executed in the same manner as a

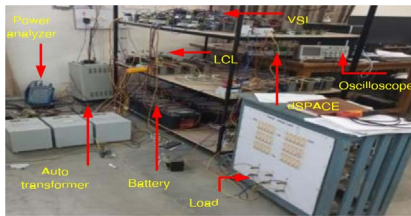


**Fig. 12.** Hardware setup.

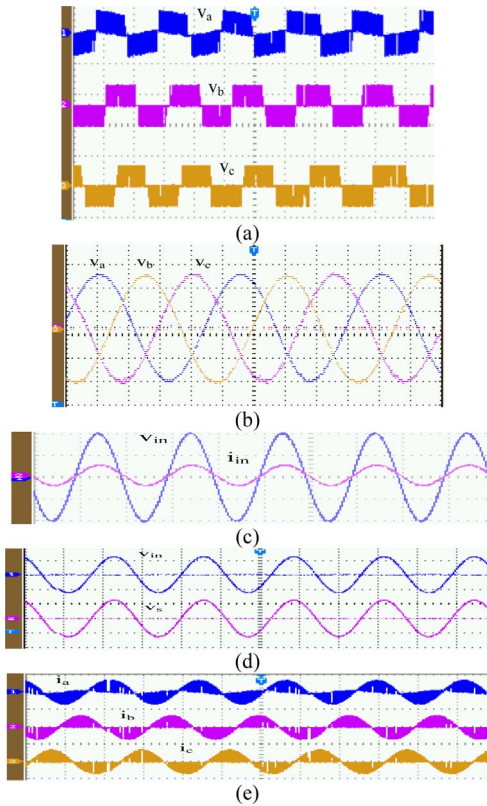


**Fig. 13.** OPAL-RT results (a) inverter line voltage (V) (before filter), (b) inverter three-phase voltages (V) after the filter, (c) line voltage (V) and current (A), (d) inverter line voltage (V) and grid voltage (V) and (e) 3-phase currents (A).

physical system. The Matlab/Simulink system interacts with the OPAL-RT simulator using the RT-Lab software. The simulator implements hardware-in-loop (HIL), control-in-loop (CIL), and real-time simulation. In this paper, the DC/AC $\mu$ G developed in Simulink is performed in real-time using ARTEMiS-SSN-solver on a 3.2 GHz processor, 2.8 cores, 16 GB RAM simulator, and at a step time of 20  $\mu$ s. The solver can decouple the state space of the broad power network into lower groups; its solution can be determined simultaneously through the nodal-admittance method.

The HIL results of 3-phase voltages are displayed in Figure 13b, which perfectly matches the simulation outcome of three-phase voltages in Figure 8c. Figure 8d illustrates inverter simulation output voltage which is the same as OPAL-RT results in Figure 13a. Figure 9d shows

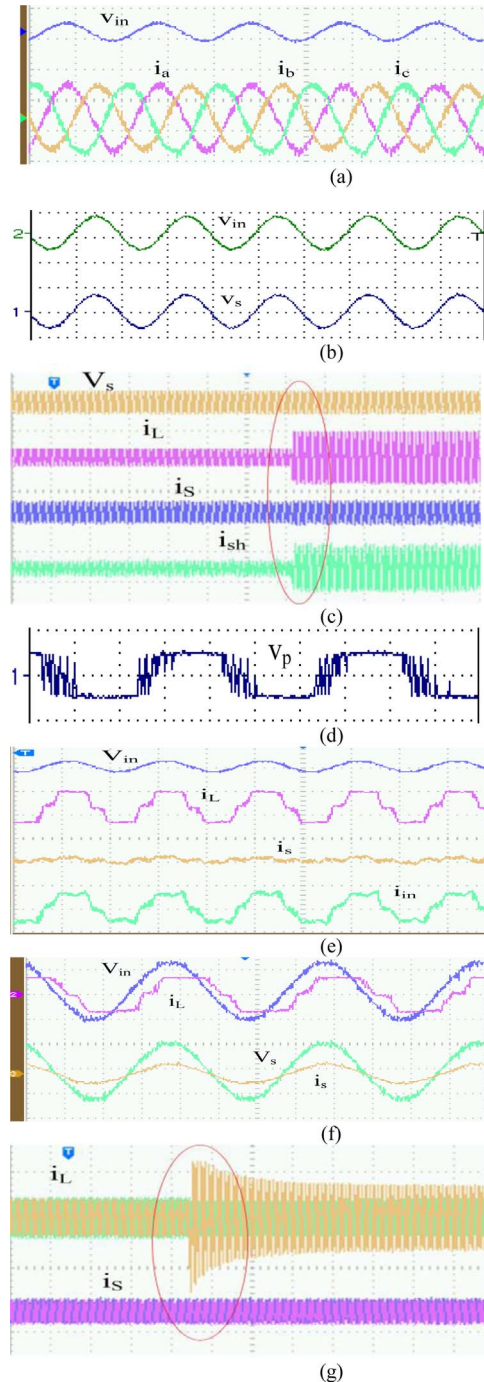


**Fig. 14.** Experimental results: (a) VSI-1 three phase currents ( $i_{abc}$ ) (scale 5 A/div) and phase voltage ( $V_{in}$ ) (scale 200 V/div), time (scale 10 ms/div), (b) inverter line voltage and grid voltage (scale 100 V/div), time (scale 10 ms/div), (c) dynamic performance under a step load change (scale of VSI-1 200 V/div) all currents (scales-5 A/div), time (scale 200 ms/div), (d) inverter pole voltage (scale 100 V/div), time (scale 5 ms/div), (e) in islanding the VSI-2 is feeding the CPL  $V_{in}$  (200 V/div), all current (5 A/div), time (scale 10 ms/div), (f) unity power factor operation  $V_{in}$  and  $V_s$  equal to (100 V/div),  $i_L$  and  $i_s$  equal to (5 A/div), time (scale 10 ms/div) and (g) dynamic performance under a step load change of VSI-2 (scale 5 A/div), time (scale 200 ms/div).

the same grid line and inverter voltage results, equivalent to those obtained in OPAL-RT results in [Figure 13d](#). Three-phase OPAL-RT currents shown in [Figure 13e](#) are symmetrical as simulation results in [Figure 10g](#).

The performance of the proposed AC/DC microgrid has been verified experimentally, and [Figure 14](#) demonstrates the same. [Figure 14a](#) indicates the inverter voltage of phase A and the three-phase inverter currents in the top to bottom order. [Figure 14b](#) depicts the inverter voltage after the filter and the source voltage. These waveforms are shown in green and blue, respectively. [Figure 14c](#) captures the dynamic performance of VSI-1 by initiating CPL-2. Thus, the load current increases; however, the source current remains constant, and the DC-bus provides the step power. The experimental results show the capability of the DC–DC converter in peak load management. [Figure 14d](#) shows the pole voltage of VSI-1 before the LCL filter. [Figure 14e](#) shows the proposed microgrid operation in islanding mode. The inverter voltage, load current of CPL, source current, and the inverter current are shown subsequently top first. [Figure 14f](#) shows inverter voltage and load current at the top, whereas the bottom shows source voltage and source current. These results manifest that the VSI-1 can mitigate power quality problems. [Figure 14g](#) shows a dynamic performance of VSI-2 when CPL-2 is switched on, and thus load current is increased. However, the source current from the grid side remains constant. Thus it demonstrates the plug-and-play features of the microgrid.

## 6 Conclusion

In this work report, a decentralized-control system of AC/DC microgrid operating both in grid-interactive and islanding mode is simulated in MATLAB/Simulink and tested using the OPAL-RT digital simulator, followed by experimental verification. The hybrid DC/AC  $\mu$ G is interfaced with distributed generation (PMSG wind turbine, solar PV), AC loads, DC loads, ICs, battery energy storage system, and AC grid. The fast-tracking efficient energy MPPT with droop control is deployed for solar PV and PMSG-based wind turbines with BESS systems. The distinct features such as power control, frequency droop control, current control, and P/Q control are illustrated. The BESS smoothes the DC-link voltage and keeps the power invariant under variations in load, solar irradiance, and wind speed. The DC-link voltage is maintained within the acceptable range with the help of BESS in islanding mode and bidirectional AC/DC converter in grid connected mode. The control strategies proposed in the system function outside of online communication between different DGs. The real-time waveforms and simulation results show the proposed DC/AC  $\mu$ G controller that efficiently performs power-sharing among two interlinking converters and supplies/receives quality power to/from the grid. In addition, the power exchange between the microgrid and utility is achieved with good power quality as mentioned in IEEE 519-2014 standards. Droop control is added in the feedback current to a voltage and current inner loops of wind and solar PV units, developing a synthetical

output impedance in the individual converter. Experimental results demonstrate that the power quality at the PCC is sustained within the grid standard. LCL filter is optimally designed to enhance the system's power quality with damping. Stability analysis also reported in [Section 3](#) validates the stability and efficacy of the proposed microgrid. Hence, this work reports the recommended DC/AC  $\mu$ G architecture's versatility and usefulness of the decentralized control methods.

*Acknowledgments.* The authors thank Arkabrata Dattaroy for the extensive editing and overview of the paper.

## References

- Xu Q., Xiaolei H., Wang P., Xiao J., Pengfei T., Wen C., Lee M.Y. (2016) A decentralized dynamic power-sharing strategy for hybrid energy storage system in autonomous DC microgrid, *IEEE Trans. Ind. Electron.* **64**, 7, 5930–5941.
- Yi Z., Dong W., Etemadi A.H. (2017) A unified control and power management scheme for PV-battery-based hybrid microgrids for grid-connected and islanded modes, *IEEE Trans. Smart Grid* **9**, 6, 5975–5985.
- Fakenham H., Lu D., Francois B. (2010) Power control design of a battery charger in a hybrid active PV generator for load-following applications, *IEEE Trans. Ind. Electron.* **58**, 1, 85–94.
- Tammara N.R., Mishra M.K., Srinivas S. (2015) Dynamic energy management of renewable grid integrated hybrid energy storage system, *IEEE Trans. Ind. Electron.* **62**, 12, 7728–7737.
- Xiao J., Wang P., Setyawan L. (2015) Hierarchical control of hybrid energy storage system in DC microgrids, *IEEE Trans. Ind. Electron.* **62**, 8, 4915–4924.
- Yang P., Yu M., Wu Q., Hatziargyriou N., Xia Y., Wei W. (2019) Decentralized bidirectional voltage supporting control for multi-mode hybrid AC/DC microgrid, *IEEE Trans. Smart Grid* **11**, 3, 2615–2626.
- Garcia P., Arbolea P., Mohamed B., Vega A.A.C. (2016) Implementation of a hybrid distributed/centralized real-time monitoring system for a DC/AC microgrid with energy storage capabilities, *IEEE Trans. Ind. Inform.* **12**, 5, 1900–1909.
- Pena-Alzola R., Liserre M., Blaabjerg F., Ordonez M., Yang Y. (2014) LCL-filter design for robust active damping in grid-connected converters, *IEEE Trans. Ind. Inform.* **10**, 4, 2192–2203.
- Photovoltaics D.G., Storage E. (2005) *IEEE Standard Conformance Test Procedures for Equipment Interconnecting Distributed Resources with Electric Power Systems*. IEEE Std 1547.1-2005. IEEE Standards Coordinating Committee 21.
- Wang C., Li X., Guo L., Li Y.W. (2014) A nonlinear-disturbance-observer-based DC-bus voltage control for a hybrid AC/DC microgrid, *IEEE Trans. Power Electron.* **29**, 11, 6162–6177.
- Liu X., Wang P., Loh P.C. (2011) A hybrid AC/DC microgrid and coordination control, *IEEE Trans. Smart Grid* **2**, 2, 278–286.
- Issa W.R., El Khateb A.H., Abusara M.A., Mallick T.K. (2017) Control strategy for uninterrupted microgrid mode transfer during unintentional islanding scenarios, *IEEE Trans. Ind. Electron.* **65**, 6, 4831–4839.

- 13 Li X., Guo L., Li Y., Guo Z., Hong C., Zhang Y., Wang C. (2017) A unified control for the DC–AC interlinking converters in hybrid AC/DC microgrids, *IEEE Trans. Smart Grid* **9**, 6, 6540–6553.
- 14 Tan K.T., Peng X.Y., So P.L., Chu Y.C., Chen M.Z. (2012) Centralized control for parallel operation of distributed generation inverters in microgrids, *IEEE Trans. Smart Grid* **3**, 4, 1977–1987.
- 15 Mazumder S.K., Tahir M., Acharya K. (2008) Master-slave current-sharing control of a parallel DC–DC converter system over an RF communication interface, *IEEE Trans. Ind. Electron.* **55**, 1, 59–66.
- 16 Mahmood H., Michaelson D., Jiang J. (2015) Decentralized power management of a P.V./battery hybrid unit in a droop-controlled islanded microgrid, *IEEE Trans. Power Electron.* **30**, 12, 7215–7229.
- 17 Liang B., Kang L., He J., Zheng F., Xia Y., Zhang Z., Zhang Z., Liu G., Zhao Y. (2019) Coordination control of hybrid AC/DC microgrid, *J. Eng.* **16**, 3264–3269.
- 18 Zhou Q., Shahidehpour M., Paaso A., Bahramirad S., Alabdulwahab A., Abusorrah A. (2020) Distributed control and communication strategies in networked microgrids, *IEEE Commun. Surv. Tutor.* **22**, 4, 2586–2633.
- 19 Wu D., Tang F., Dragicevic T., Vasquez J.C., Guerrero J.M. (2015) A control architecture to coordinate renewable energy sources and energy storage systems in islanded microgrids, *IEEE Trans. Smart Grid* **6**, 3, 1156–1166.
- 20 Loh P.C., Li D., Chai Y.K., Blaabjerg F. (2012) Autonomous operation of hybrid microgrid with AC and DC subgrids, *IEEE Trans. Power Electron.* **28**, 5, 2214–2223.
- 21 Guerrero J.M., Vasquez J.C., Matas J., De Vicuña L.G., Castilla M. (2011) Hierarchical control of droop-controlled AC and DC microgrids—A general approach toward standardization, *IEEE Trans. Ind. Electron.* **58**, 1, 158–172.
- 22 Majumder R., Chaudhuri B., Ghosh A., Majumder R., Ledwich G., Zare F. (2009) Improvement of stability and load sharing in an autonomous microgrid using supplementary droop control loop, *IEEE Trans. Power Syst.* **25**, 2, 796–808.
- 23 Tian H., Wen X., Li Y.W. (2018) A harmonic compensation approach for interlinking voltage source converters in hybrid AC–DC microgrids with low switching frequency, *CSEE J. Power Energy Syst.* **4**, 1, 39–48.
- 24 Issa W., Sharkh S., Mallick T., Abusara M. (2016) Abusara: Improved reactive power-sharing for parallel-operated inverters in islanded microgrids, *J. Power Electron.* **16**, 3, 1152–1162.
- 25 Amirkhan S., Radmehr M., Rezanejad M., Khormali S. (2020) A robust control technique for stable operation of a DC/AC hybrid microgrid under parameters and loads variations, *Int. J. Electr. Power Energy Syst.* **117**, 105659.
- 26 Antalem D.T., Bhattacharya A. (2020) Decentralized control for grid-interactive hybrid DC/AC ring microgrid under input source fluctuations, in: *2020 IEEE International Conference on Computing, Power and Communication Technologies (GUCON)*, 2–4 October 2020, Greater Noida, India, pp. 383–388.
- 27 Elgendi M.A., Zahawi B., Atkinson D.J. (2011) Assessment of perturb and observe MPPT algorithm implementation techniques for PV pumping applications, *IEEE Trans. Sustain. Energy* **3**, 1, 21–33.
- 28 Kirakosyan A., El-Saadany E.F., El Moursi M.S., Yazdavar A.H., Al-Durra A. (2019) Communication-free current sharing control strategy for DC microgrids and its application for AC/DC hybrid microgrids, *IEEE Trans. Power Syst.* **35**, 1, 140–151.
- 29 Rahim A.P.N., Pagano D.J., Lenz E., Stramosk V. (2014) Modeling and stability analysis of islanded DC microgrids under droop control, *IEEE Trans. Power Electron.* **30**, 8, 4597–4607.
- 30 Delghavi M.B., Yazdani A. (2010) Islanded-mode control of electronically coupled distributed-resource units under unbalanced and nonlinear load conditions, *IEEE Trans. Power Deliv.* **26**, 2, 661–673.
- 31 Alrajhi Alsiraji H. (2019) A new virtual synchronous machine control structure for voltage source converter in high voltage direct current applications, *Umm, Al Qura Univ. J. Eng. Archit.* **11**, 1, 1–6.
- 32 Selman N.H., Mahmood J.R. (2016) Comparison between perturb & observe, incremental conductance and fuzzy logic MPPT techniques at different weather conditions, *Int. J. Innov. Res. Technol. Sci. Eng.* **5**, 7, 12556–12569.
- 33 Alsiraji H.A., El-Shatshat R. (2021) Virtual synchronous machine/dual-droop controller for parallel interlinking converters in hybrid AC–DC microgrids, *Arab. J. Sci. Eng.* **46**, 2, 983–1000.